Int. J. Multiphase Flow Vol. 12, No. 1, pp. 35–61, 1986
Printed in Great Britain.

0301-9322/86 $3.00 + .00
Pergamon/Elsevier

VORTICES IN BUBBLY TWO-PHASE FLOW

THOMAS L. COOK†
Earth and Space Sciences Division, Los Alamos National Laboratory, Los Alamos, NM 87545, U.S.A.

and

FRANCIS H. HARLOW
Theoretical Division, Los Alamos National Laboratory, Los Alamos, NM 87545, U.S.A.

(*Received* 18 *July* 1984; *in revised form* 30 *April* 1985)

Abstract—The properties of a von Kármán vortex street are examined theoretically for bubbly flow around a rectangular obstacle. The time-dependent, two-dimensional Navier–Stokes equations describing each field are coupled through local pressure equilibration, a phenomenological momentum exchange term and a new representation of the virtual mass acceleration terms. Bubble fragmentation and coalescence are represented by the effect of relaxation to local Weber number equilibrium in a transport equation for the time and space variations of bubble-number density. Turbulence is represented by an eddy viscosity model. High-speed computer results for an air–water system agree well with published data for downstream gas accumulation in the vortices. Variations in Strouhal frequency with upstream void fraction are discussed in terms of bubble sublayer growth along the sides of the obstacle and the resulting movement of the flow separation streamline. Satellite eddy formation is observed, and the alteration of street characteristics by bubble migration is examined.

1. INTRODUCTION

The periodic shedding of vortices from alternate sides of an obstacle in a fluid stream has been studied for almost one hundred years. Experimental observations of vibrations excited in wires by the flow of air were first reported by Strouhal (1878). Alhborn (1902) used visualization techniques to show the characteristic pattern of alternating vortices. A theory describing the vortex street in an infinite medium was first published by von Kármán & Rubach (1912).

Since these early investigations, von Kármán vortex streets in circumstances involving only single-field flow have been extensively studied, both experimentally and theoretically. Roshko (1954) summarizes the results of the many experimental studies of right circular cylinders. Fage & Johansen (1927) present experimental results for a flat plate inclined at various angles to the flow. Bearman & Obasaju (1982) have studied fixed and oscillating square-section cylinders. Theoretical studies using real configurations have been accomplished through the means of powerful numerical solution techniques, Fromm & Harlow (1963) and Harlow & Fromm (1964).

For single-phase flow around a single obstacle, the fluid dynamics is characterized by several properties that have been examined in detail by experimentalists and theorists. For aerodynamical applications, the principal considerations are those of drag and lift. For blunter obstacles, such as those considered in this paper, the properties of drag and lift may also be of interest. However, the dominant feature is the periodic shedding of the vortices. The shedding is characterized by a dimensionless Strouhal number, $S \equiv fd/v$, where f is the frequency of the street (i.e. the inverse of the time between the shedding of successive vortices on any one side of the obstacle), d is the cross-stream obstacle width, and v is the inlet velocity of the liquid. For Reynolds numbers (based on the cross-stream length of the obstacle and the molecular viscosity) less than a critical value of about 40, the flow pattern is steady; and the shedding frequency is not an issue. As the Reynolds number increases above 40, the Strouhal number increases to an asymptotic value of about 0.2. Even for Reynolds numbers above several hundred, when turbulence is noticeable, the dominant frequency

---

†Present affiliation: S-CUBED Division of Maxwell Laboratories, Inc., San Diego, CA 92038, U.S.A.

nevertheless corresponds to an S of about 0.2. As shown by Roshko (1954), this dominance persists for circular cylinders to Reynolds numbers as high as 8000.

Recently, investigators have begun to examine the inception and evolution of von Kármán vortex streets in multifield flows. A theory for the motion of individual bubbles in unsteady nonuniform flows has been developed and applied by Thomas *et al.* (1983) to the special case of bubble entrapment and by a line vortex. An experimental study of vortex shedding for the vertical flow of an air–water system past blunt bodies has been published by Hulin *et al.* (1982). Theoretical studies of the same configuration have been described by Cook & Harlow (1984a) who use a numerical solution technique based upon a two-field approximation.

The purpose of this paper is to examine the microphysical modeling described by the two-field equations and to summarize the properties of a von Kármán street in this type of bubbly flows.

2. BASIC TWO-FIELD EQUATIONS

We write the ensemble-averaged, two-field equations for one phase dispersed in another. Either phase can be any one of the different states of matter (gas, liquid or solid), but in the present study we examine the case in which the dispersed material is a gas (air), and the continuous phase is a liquid (water). In this treatment, both fields are accelerated by variations of the same pressure. Because our calculations extend only over small spatial intervals, a meter or so, the microscopic densities, ρ_L and ρ_G, can be considered constant.

In the absence of mass exchange between the phases, the continuity equations are

$$\frac{\partial \rho'_L}{\partial t} + \nabla \cdot (\rho'_L \mathbf{u}_L) = 0 \qquad [1]$$

and

$$\frac{\partial \rho'_G}{\partial t} + \nabla \cdot (\rho'_G \mathbf{u}_G) = 0, \qquad [2]$$

where ρ'_L is the macroscopic density of the continuous phase, ρ'_G is the macroscopic density of the dispersed phase; and $\mathbf{u}_L$ and $\mathbf{u}_G$ are the respective velocities of the continuous and dispersed phases.

It is more convenient to work directly with the volume fractions of the two phases. We define

$$\rho'_L \equiv \rho_L \alpha_L \qquad [3]$$

and

$$\rho'_G \equiv \rho_G \alpha_G, \qquad [4]$$

where α_L and α_G are the volume fractions of the continuous and dispersed phases, respectively. For constant microscopic densities, the mass-conservation equations become

$$\frac{\partial \alpha_L}{\partial t} + \nabla \cdot (\alpha_L \mathbf{u}_L) = 0 \qquad [5]$$

and

$$\frac{\partial \alpha_G}{\partial t} + \nabla \cdot (\alpha_G \mathbf{u}_G) = 0. \qquad [6]$$

In general, $\alpha_L + \alpha_G = 1$.

The momentum equations are written in terms of volume fractions with the microscopic densities factored outside of the derivatives.

$$\rho_L\left[\frac{\partial \alpha_L \mathbf{u}_L}{\partial t} + \nabla \cdot (\alpha_L \mathbf{u}_L \mathbf{u}_L)\right] = -\alpha_L \nabla p + \rho_L \alpha_L \mathbf{g} + K(\mathbf{u}_G - \mathbf{u}_L) + \rho_L \mathbf{V}_L + \mathbf{M}_L \qquad [7]$$

and

$$\rho_G\left[\frac{\partial \alpha_G \mathbf{u}_G}{\partial t} + \nabla \cdot (\alpha_G \mathbf{u}_G \mathbf{u}_G)\right] = -\alpha_G \nabla p + \rho_G \alpha_G \mathbf{g} + K(\mathbf{u}_L - \mathbf{u}_G) + \rho_G \mathbf{V}_G + \mathbf{M}_G. \qquad [8]$$

The pressure is p, the gravitational acceleration, $\mathbf{g}$. The quantity K is a function that describes the interfacial momentum exchange between the fields. The effective viscous stress terms (both molecular and turbulent) for the continuous and dispersed phases are $\mathbf{V}_L$ and $\mathbf{V}_G$, respectively; the virtual mass terms are $\mathbf{M}_L$ and $\mathbf{M}_G$. The momentum exchange function and the viscous stress and virtual mass terms are discussed in detail below.

Because of the uncertainty with regard to swarming effects, we have intentionally included only the principal drag terms—omitting such possibly contributory terms as the vorticity-lift force, the lift and drag modifications due to shape distortion, the Bassett terms, and the nonsteady contributions to the flow-separation Taylor–Davies drag. Certainly, the effects represented by these terms will ultimately need serious consideration. These studies are anticipated to constitute further directions for our research.

3. INTERACTION MODELS

A. *Virtual mass effect*

In the two-phase motion of a bubble through a liquid, the total effective mass of the bubble consists of the vapor itself plus a virtual mass that arises from the inertial properties of the liquid in the immediate vicinity of the bubble. A generalized formulation of the virtual mass effect has been derived by Cook & Harlow (1984b). The terms for [7] and [8] are

$$\mathbf{M}_L = \frac{f_{vm}\rho_L\alpha_L\alpha_G}{(\alpha_L - f_{vm}\,\alpha_G)}\left[\frac{D_G\mathbf{u}_G}{Dt} - \frac{D_L\mathbf{u}_L}{Dt} - \frac{1}{\alpha_G}\nabla \cdot \left(\frac{\alpha_L\,\alpha_G}{(\alpha_L - f_{vm}\,\alpha_G)}\right)(\mathbf{u}_G - \mathbf{u}_L)\,(\mathbf{u}_G - \mathbf{u}_L)\right] \qquad [9]$$

and

$$\mathbf{M}_G = -\frac{f_{vm}\rho_L\alpha_L\alpha_G}{(\alpha_L - f_{vm}\alpha_G)}\left[\frac{D_G\mathbf{u}_G}{Dt} - \frac{D_L\mathbf{u}_L}{Dt} - \frac{f_{vm}}{\alpha_L}\nabla \cdot \left(\frac{\alpha_L\alpha_G}{(\alpha_L - f_{vm}\alpha_G)}\right)(\mathbf{u}_G - \mathbf{u}_L)\,(\mathbf{u}_G - \mathbf{u}_L)\right]. \qquad [10]$$

The Lagrangian time derivatives for the respective phases are given by $D_i/D_t = \partial/\partial t + \mathbf{u}_i \cdot \nabla$. The factor, f_{vm}, is a parameter analogous to the virtual volume coefficient used in classical formulations of the effect.

Under most circumstances the validity of the virtual mass concept for bubbles implies that $f_{vm}\alpha_G$ is small compared to α_L, so that the otherwise vanishing denominators in [9] and [10] are of no concern. Cook & Harlow (1984b) show that this formulation is internally conservative of momentum for an arbitrary Eulerian control volume and is mathematically objective.

B. *Momentum exchange function*

Cook & Harlow (1984a) write the interfacial momentum exchange function in the form

$$K = \frac{3}{8}\frac{C_D\rho_L\,|\,\delta\mathbf{u}\,|}{r(1/\alpha_L + 1/\alpha_G)}, \qquad [11]$$

where C_D, the drag coefficient, is a function of Reynolds number and Morton number as described in section III-D. below. The bubble radius, r, depends on the local bubble number density and the local volume fraction. $\delta\mathbf{u}$ is the relative velocity, $\mathbf{u}_G - \mathbf{u}_L$.

C. *Bubble coalescence, fragmentation and transport*

On the assumption that the bubbles are spherical and all the same size the local bubble radius is given by

$$r = (3\,\alpha_G/4\pi N)^{1/3}, \qquad [12]$$

where N is the bubble number density. In equilibrium the bubble radius would be determined by a balance of surface tension and inertial forces as described by a Weber number criterion.

$$\mathrm{We} = \frac{2\rho_L\,|\,\delta\mathbf{u}_t\,|^2}{\sigma/r_e}, \qquad [13]$$

where σ is the surface tension of the interface, r_e is the radius of the bubble in equilibrium and $\delta\mathbf{u}_t$ is the terminal rise velocity of the bubble.

Conservative transport of bubble number density is altered by the effects of coalescence and fragmentation. We postulate a single-relaxation-time model of the form

$$\partial N/\partial t + \nabla\cdot\mathbf{u}_G N = \omega_b\,(N_e - N), \qquad [14]$$

in which the single-relaxation parameter, ω_b, controls the rates for both coalescence and fragmentation and, therefore, must depend strongly on whether the local bubble size is less than r_e (the collision dominated coalescence regime) or greater than r_e (the rupture dominated fragmentation regime). More generally, the relaxation to Weber number equilibrium involves collision integrals over an appropriate two-integral distribution function together with a detailed description of bubble rupture dynamics resulting from the local forces. The complexity of these considerations is well beyond the scope of the present investigation, our immediate goal being to demonstrate which features of the flow are strongly sensitive to the choice of ω_b and which are not.

The equilibrium number density is obtained from [12]

$$N_e = 3\alpha_G/4\pi r_e^3, \qquad [15]$$

and r_e is obtained by solving [13] with a specified value for We.

D. *Drag coefficient correlation functions*

The drag coefficient that appears in [11] varies as a function of bubble Reynolds number,

$$\mathrm{Re}_b = 2r\,|\,\delta\mathbf{u}\,|\,/\nu_L, \qquad [16]$$

and Morton number,

$$G_L = |\,\mathbf{g}\,|\,\mu_L^4/\rho_L\,\sigma^3, \qquad [17]$$

where ν_L and μ_L are the kinematic and absolute viscosities, respectively, of the continuous phase. Utilizing the correlations of Peebles & Garber (1953) we write

$$C_D = 24\,\mathrm{Re}_b^{-1}, \quad \text{for } \mathrm{Re}_b < 2, \qquad [18]$$

$$C_D = 18.7\,\mathrm{Re}_b^{-0.68}, \quad \text{for } 2 \le \mathrm{Re}_b \le 4.02 G_L^{-0.214} \qquad [19]$$

and

$$C_D = 0.6145r \, | \delta \mathbf{u} | \, 1 1^{-2}, \text{ for } \mathrm{Re}_b \geq 4.02 G_L^{-0.214}. \qquad [20]$$

The three regimes represented by [18] and [19] are Stokes, oscillating bubble and Taylor–Davies, respectively. Equation [20] is a linearized combination of two higher Reynolds number regimes reported in Peebles & Garber (1953). The simplification represents the data to within a degree of accuracy that is consistent with the uncertainties in the drag function due to swarming and nonsteady flow effects and is useful because it avoids a parameter space of little interest to us in which the momentum exchange function depends on the relative velocity to the fourth power.

E. *Viscous and turbulent stress models*

The role of viscosity, as measured by the Reynolds number Re, is a crucial one in the dynamics of a von Kármán vortex street. The usual definition of Reynolds number is

$$\mathrm{Re} \equiv \bar{u} d / \nu, \qquad [21]$$

where $\bar{u}$ is the average flow speed, d is a characteristic length (in this case the cross-stream obstacle width) and ν is an appropriate kinematic viscosity.

For a single fluid moving sufficiently slowly the relevant value of ν is simply the molecular kinematic viscosity, ν_m. For higher speeds the flow Reynolds number still is usually characterized by means of the molecular viscosity, but the presence of turbulence suggests that a more relevant characterization should be based on the total effective viscosity, the sum of molecular and turbulence contributions. Following Launder & Spalding (1974), we can describe the turbulence eddy viscosity by means of the formula

$$\nu_t = C_t s \sqrt{2q}, \qquad [22]$$

where C_t is about 0.02, s is an appropriate length scale of the turbulence, and q is the fluctuational kinetic energy per unit mass. The magnitude of q can be estimated roughly as some fraction, f_t^2, of the mean flow kinetic energy per unit mass, $\frac{1}{2}\bar{u}^2$. With $\nu = \nu_t + \nu_m$ and with s expressed as some factor, f_s, of the obstacle width, the effective Reynolds number becomes

$$\mathrm{Re}_{\mathrm{eff}} = \frac{1}{C_t f_s f_t + 1/\mathrm{Re}}. \qquad [23]$$

Following a suggestion by Lessen & Singh (1974), as the Reynolds number goes to infinity, the effective Reynolds number is bounded to a value that can be estimated as a few hundred. Since the Strouhal number is likewise bounded as a function of Reynolds number, it is perhaps more appropriate to examine the variations of Strouhal number with effective Reynolds number.

For two-phase flow, the concept of Reynolds number becomes more complicated for several reasons. The presence of dispersed entities (e.g., bubbles, droplets or particles) has a significant influence on the effective viscosity, even when the flow is laminar. At higher speeds as in the present investigation, the nature of the turbulence is expected to be profoundly modified in several ways. There are at least two potential sources for turbulence creation, one from the fluctuations in the wakes of the individual entities and the other from the propensity to instability of the two-phase flow whenever there is appreciable relative motion between the fields.

For single-phase flow the representation of turbulence can be formulated to any of a variety of degrees of complexity. The simplest approach is to postulate a constant prescribed eddy viscosity. Mixing length theories belong to the next level of complexity. In general, however, we require equations describing the time-dependent transport of the turbulence. Transport equations for the Reynolds stress, R_{ij}, are conceptually the most satisfactory approach. Simpler formulations, for example the $k - \epsilon$ model, describe the transport of purely scalar quantities (the turbulence energy density and dissipation rate).

For our two-phase flow calculations, our approach is to investigate a succession of models commencing with the simplest description, which utilizes an eddy viscosity given by [22]. The viscous and turbulent stresses are, therefore, included by writing

$$\mathbf{V}_L = (\nabla \cdot \nu\alpha_L\nabla)\mathbf{u}_L \qquad [24]$$

and

$$\mathbf{V}_G = (\nabla \cdot \nu\alpha_G\nabla)\mathbf{u}_G. \qquad [25]$$

Despite the simplicity of this model there is much to learn by its utilization, and comparisons between calculational results and experimental data are surprisingly good. Subsequent studies of this problem will rely on two-phase turbulence transport equations such as those of Besnard & Harlow (1985a,b)

4. NUMERICAL PROCEDURE

A. *Solution technique*

The equations are written in finite-difference form, and the variables are advanced through time by a series of discrete steps. The methodology is similar to other schemes that we have used in two-field flows and is described in detail elsewhere (Cook & Harlow 1984a).

Each computational cycle consists of several solution phases. In phase 1 the convection, viscous stress, and spatial part of the virtual mass terms are calculated explicitly. In phase 2 the velocities, volume fractions, and pressures are obtained by an iterative procedure designed to allow pressure effects to propagate over the entire calculational mesh, a standard procedure for the treatment of incompressible fluids, as described by Harlow & Amsden (1975). In phase 3 we use a corrective procedure to tighten the convergence of the sum of the volume fractions to unity, and we update the old variables in anticipation of the next time cycle.

The discretization techniques used in this methodology are a mixture of cell-centered and donor-cell differencing schemes. Donor-cell differencing is used in the solution of the continuity equations and of the bubble number transport equation, where it automatically adds a small amount of artificial diffusion comparable in magnitude and opposite in sign to the lowest order truncation-error terms (Hirt 1968). The momentum equations are discretized using cell-centered differencing for the convection terms to avoid the excessive truncation-error viscosity arising from the donor-cell procedure and the resulting damping of the von Kármán vortex street.

B. *Geometry and boundary conditions*

The bubbly Kármán vortex street to which this present research is directed can be modeled with a two-dimensional rectangular coordinate system. We visualize a conduit in which a single object has been placed across the fluid flow. Figure 1 illustrates this geometry.

The bottom is an inlet boundary where upstream-flow conditions are imposed by specifying v_i^{in} and α_i^{in}. Because the principal effect of these boundary conditions is manifested

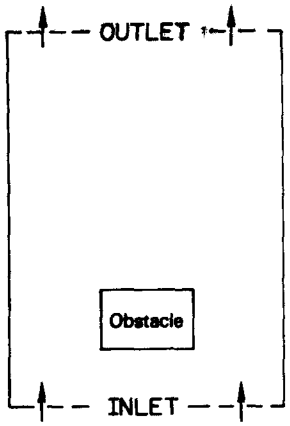

Figure 1. Typical conduit geometry.

variables reflects the use of donor-cell convection for the volume fraction equations and centered convection for the momentum equations. The top is an outlet boundary. The velocities at this upper boundary are normalized to guarantee mass conservation and to ensure local continuity of the flow.

Representation of the boundary conditions at the rigid walls of the conduit and obstacle requires a consideration of the probable boundary layer thickness that can be expected at those walls. If the boundary layer thickness is small compared to the dimensions of a calculational cell, then it is appropriate to use free-slip boundary conditions at the wall. The use of no-slip boundary conditions is appropriate only for those circumstances in which the boundary layer can be resolved. The thickness of a laminar boundary layer is expected to be small on both the obstacle and conduit walls for most circumstances of interest in this study. Turbulent boundary layer thickness is less amenable to precise characterization. On the obstacle we still expect the boundary layer to be small and are currently assuming this to be also the case on the conduit walls. Thus, the normal gradient of the tangential velocity vanishes. In addition, the normal component of the velocity and the gradient of any scalar variable vanish.

The use of free-slip boundary conditions on the obstacle does not, however, preclude the shedding of vorticity that is crucial to the formation of a vortex street. The details of the vortex production immediately downstream of an obstacle are determined by the location of the flow separation points. For a long rectangular obstacle these points are the aft corners. For a short rectangular obstacle the flow separation at the forward corners may also be of significance for the production of vorticity. The vorticity created by the separated flow at the aft corners is properly represented by the velocity jump between the external and wake flow regions; for the forward corners proper representation of the vortex shedding may require very fine resolution in the finite-difference calculations.

C. *Initial conditions*

The nature of the initial conditions is such that they have no physical reality; hence, the transient stage of the solution preceding the regular oscillatory stage has no meaning. We assign inlet conditions everywhere in the calculational mesh and perturb the flow in a single cell located seven obstacle widths from the downstream left-hand edge of the obstacle. The perturbation hastens the development of the street.

5. CALCULATIONAL RESULTS

A. *Problem definition*

Four computer simulations are compared and identified as runs 1, 2, 3 and 4. The initial and boundary conditions for each run differ from those of the base case, run 2, in only one significant way. Run 1 models a shorter channel to investigate the effect of the truncated calculational grid on the street. In run 3 we widen the channel to examine the dependence of street properties on blockage ratio, which is defined as obstacle width, d, divided by channel width, W. Run 4 has the same channel dimensions as run 2, but uses a slower equilibrium relaxation rate, ω_b, for bubble fragmentation and coalescence. The value of ω_b chosen for runs 1, 2 and 3 corresponds to a rapid relaxation to local conditions relative to the expected period of the street. That is, if local conditions are conducive to fragmentation or coalescence, the bubble-size adjustment occurs on a time scale that is short relative to the period. The value chosen in run 4 corresponds in contrast to a relaxation time that is long compared to the oscillatory period.

The geometry used in all four runs is shown in figure 1. The cross-stream width of the obstacle is 3 cm; the downstream thickness is 2.5 cm. The upstream edge of the obstacle is 4.5 cm from the inlet. Flow is vertical with gravity downward.

To specify input conditions in the flow field below the obstacle, we must consider the question of bubble-size equilibrium in somewhat more detail. For the purpose of discussion, we recognize the existence of a bubble insertion point, which lies far below the inlet boundary shown in figure 1. Two ranges in bubble size must be considered. If the inserted bubbles have a radius less than the equilibrium radius, the relaxation parameter ω_b is controlled by coalescence, which depends on the collision frequency. If the probable number of collisions between the insertion point and the inlet boundary is small, almost no coalescence occurs, and the inlet bubble radius does not differ from the arbitrarily specified insertion value. If, however, the collision frequency is not small the inlet value of r cannot be arbitrarily selected and must satisfy consistency conditions among r_e, We, $\delta\mathbf{u}_t$, N_e and α_G. These conditions are the Weber number equilibrium,

$$r_e = \sigma \mathrm{We}/2\rho_L(\delta\mathbf{u}_t)^2,$$

the geometrical relationship,

$$r_e = (3\alpha_G/4\pi N_e)^{1/3},$$

and the balance equation between buoyancy and drag,

$$r_e = f(\delta\mathbf{u}_t),$$

in which $f(\delta\mathbf{u}_t)$ is determined from bubble rise data.

If the initial bubble radius is greater than r_e, the relaxation rate is controlled by fragmentation processes that may occur on a shorter time scale than the collisions. In this case it is important to select a self-consistent set of upstream inlet conditions.

For the examples discussed here, we assume that the bubble radius has indeed equilibrated during the traverse from insertion to inlet. Incoming bubbles have an inlet radius of 0.2 cm. The upstream volume fraction is 10%, a midrange value chosen for comparison with the data of Hulin *et al.* (1984). The bubbles move relative to the incoming liquid at a rate of 25 cm/s. This radius, volume fraction, and relative velocity are consistent for a critical Weber number of 3.6.

The parameters used in our turbulence model are assigned as follows: for C_t, [22], we estimate a value of 0.019; for f_t^2, [23], a value of 0.1 and for f_s, [23], a value of 0.5. The resulting effective Reynolds number is 333. The molecular Reynolds number is 27,000, based on the molecular kinematic viscosity of water, an inlet liquid flow rate of 90 cm/s and an obstacle width of 3 cm.

The virtual volume coefficient, f_{vm}, is expected to be in the range 0.0–0.5. To determine the apparent magnitude, we calculated the maximum bubble concentration in downstream vortices resulting from an inlet volume fraction of 2.82% and found that the value $f_{vm} = 0.25$

Table 1. Parameters studied in the calculations

	L (cm)	W (cm)	ω_b (s^{-1})
Run 1	42	15	20
Run 2	51	15	20
Run 3	51	18	20
Run 4	51	15	4

resulted in good agreement with the measurements of Hulin *et al.* (1982). In the expectation that this coefficient should not depend on the upstream volume fraction, we calculated the bubble concentration for several other inlet volume fractions and found the agreement between our predictions and Hulin's observations to be good.

The parameters that are varied in the four calculations are summarized in table 1, in which W is the width of the channel, L is the length of the channel and ω_b is the bubble number relaxation rate.

B. *Characterization of the results*

Several representations of the field variables are used to characterize the flow. Scalar quantities are summarized in two-dimensional, computer-generated contour plots at selected times (figures 2–6). In the plots local maxima are indicated by +'s. The pressures plotted are

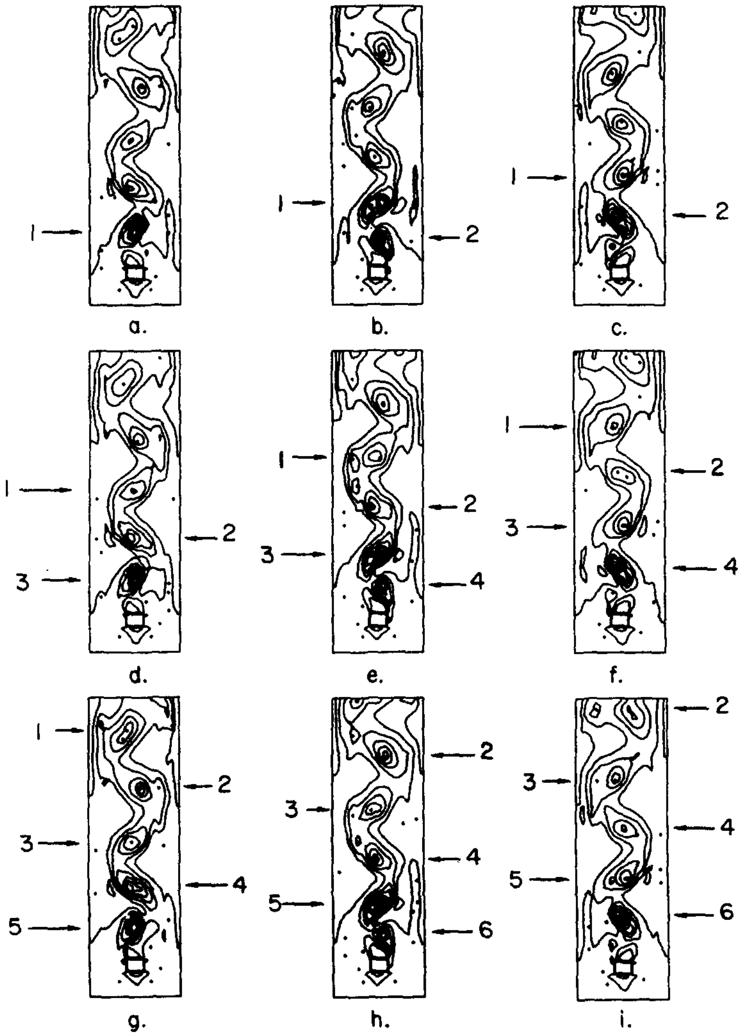

Figure 2. Contour plots of air volume fraction at equal time intervals. (a) $t = 2.410$ sec, (b) $t = 2.475$ sec, (c) $t = 2.540$ sec, (d) $t = 2.605$ sec, (e) $t = 2.670$ sec, (f) $t = 2.735$ sec, (g) $t = 2.800$ sec, (h) $t = 2.865$ sec, (i) $t = 2.930$ sec.

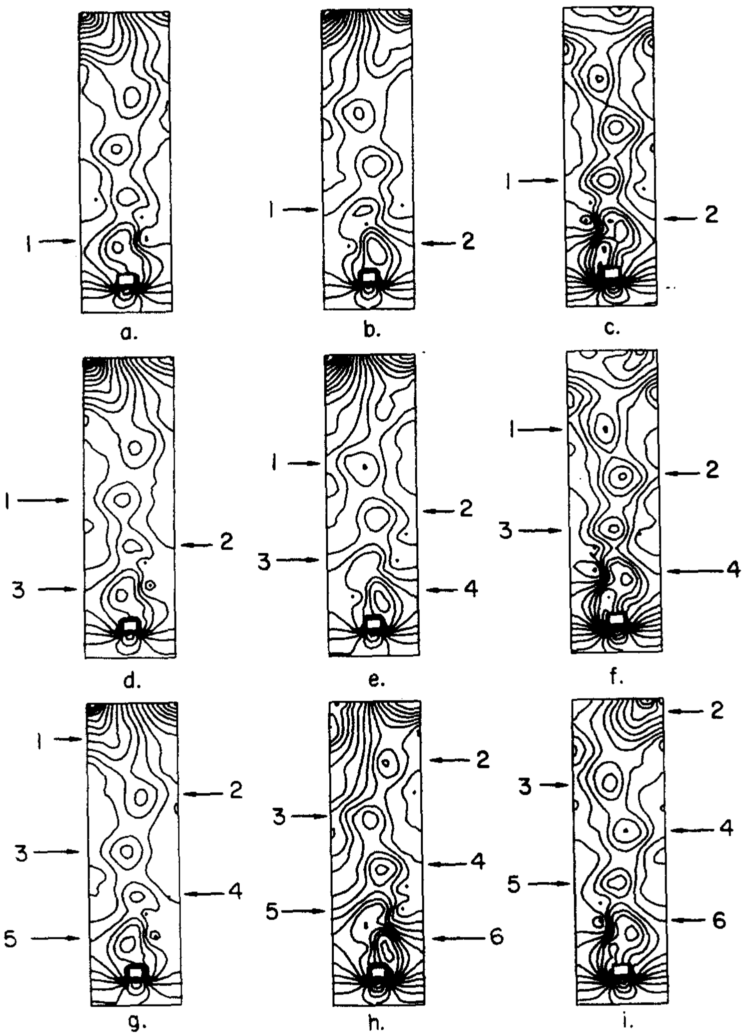

Figure 3. Contour plots of dynamic pressure at equal time intervals. (a) $t = 2.410$ sec, (b) $t = 2.475$ sec, (c) $t = 2.540$ sec, (d) $t = 2.605$ sec, (e) $t = 2.670$ sec, (f) $t = 2.735$ sec, (g) $t = 2.800$ sec, (h) $t = 2.865$ sec, (i) $t = 2.930$ sec.

the dynamic pressures, pressures from which we have subtracted the mean buoyancy for each horizontal layer.

Two-dimensional velocity vector plots are presented for each field in figures 7 and 8. During the calculation the velocity vectors are interface-centered quantities; but for the purpose of plotting, the vectors are averaged so that they can be presented at cell centers. To determine the flow direction one aligns the vector tails, which lie on vertical and horizontal lines passing through the cell centers. To enhance vortex visualization, the velocities for both the water and air fields are referred to a reference frame moving with the inlet water velocity.

Another useful way to represent the variables is with time-history plots (figure 9). At selected spatial locations we present the time histories of α_G, u_L and two different pressure differences. These times histories are helpful in identifying the end of the transient phase of the simulation. At early times the shedding frequency is not constant, and the amplitude of oscillation of the various variables changes. Properties of the Kármán street are studied and summarized after this initial phase has ended. In particular, the dependence of Strouhal frequency on upstream volume fraction is summarized in figure 10.

Another way in which we summarize the flow is by tracking individual vortices in time and in space. We follow the histories of α_G, N, K, r and p in a particular vortex from the time

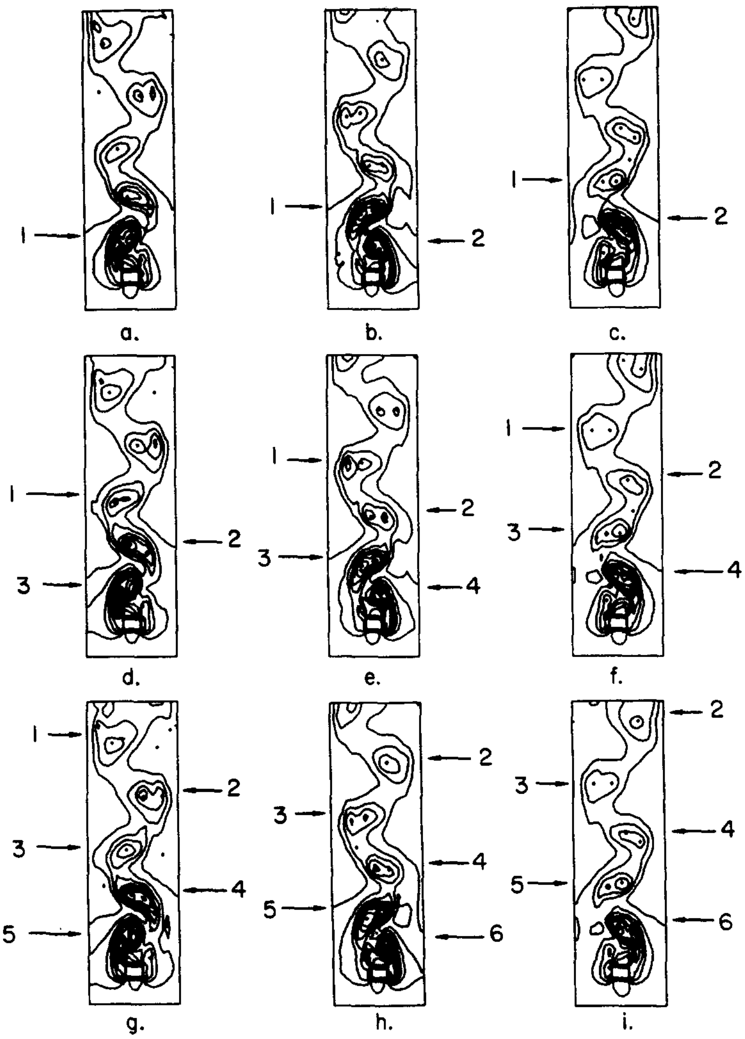

Figure 4. Contour plots of bubble number density at equal time intervals. (a) $t = 2.410$ sec, (b) $t = 2.475$ sec, (c) $t = 2.540$ sec, (d) $t = 2.605$ sec, (e) $t = 2.670$ sec, (f) $t = 2.735$ sec, (g) $t = 2.800$ sec, (h) $t = 2.865$ sec, (i) $t = 2.930$ sec.

it originates at the obstacle to the time it flows out the end of the channel. Figure 11 shows α_G as a function of time, while figures 12–16 show α_G and the other field variables as functions of position.

C. *Description of the base calculation*

The contour plots shown in figures 2–6 and the velocity vector plots in figures 7 and 8 summarize the evolution of the von Kármán vortex street that developed in our base calculation, run 2. We show plots of the scalar variables at nine times, selected so that we can identify the main properties and structural features of the two-phase street. Arrows lying outside of the plots indicate the positions of the vortices that enter into our discussions. These positions have been marked in figure 2 to indicate for each vortex the downstream location of its local maximum of gas volume fraction. Precisely, these same localities have also been marked on figures 3–8 in order to give a visual indication of slight lags or leads in the other field variables relative to the maxima of α_G. Vortices created on the left or right side of the obstacle are identified by arrows on their respective sides.

Figures 2–6 present the contour patterns of α_G, p, N, r and K at a sequence of evenly spaced times that have been chosen so that they are not perfectly in phase with the shedding of the vortices and, therefore, illustrate the street at a variety of different stages in its

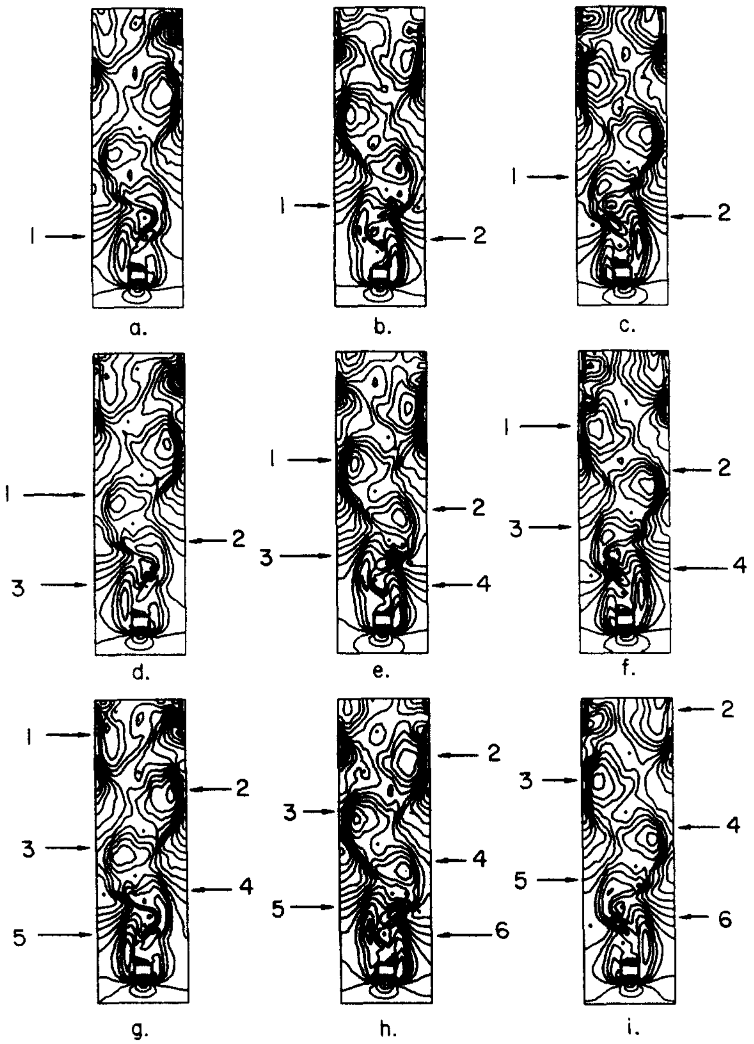

Figure 5. Contour plots of bubble radius at equal time intervals. (a) $t = 2.410$ sec, (b) $t = 2.475$ sec, (c) $t = 2.540$ sec, (d) $t = 2.605$ sec, (e) $t = 2.670$ sec, (f) $t = 2.735$ sec, (g) $t = 2.800$ sec, (h) $t = 2.865$ sec, (i) $t = 2.930$ sec.

evolution. The contour plots show that there is a close correlation among the maxima and/or minima of all the field variables in association with each particular vortex. In addition the velocity vectors in figures 7 and 8 show that these vortex positions correlate well with the location of sharp turns for both the gas and liquid velocity fields.

Consider now the stages in development and propagation of each new vortex. Vortex 5 illustrates the process especially well. Its incipient formation is just becoming visible in frame *f* of figures 2–6. In particular, figure 4(f) shows a distinct increase in the bubble number density on the left-hand side of the obstacle even before there is an appreciable buildup of gas volume fraction in figure 2(f). The bubble radius as shown in figure 5(f) is simultaneously developing a significant minimum on the left-hand side of the obstacle as a result of the same shear forces that are working to increase the number of bubbles per unit volume. In this regard it should be noted, however, that at any evolutionary stage the shear processes at the leading corners of the obstacle rupture the bubble into a local minimum that persists with some oscillation on both sides. The presence of this shear mechanism is further confirmed in reference to figure 6, which illustrates persistent local maxima in the momentum exchange rate between fields at the leading corners. Frames *g* of the figures 2–6 show the full development of vortex 5 whose incipient appearance was noted at the stage illustrated in

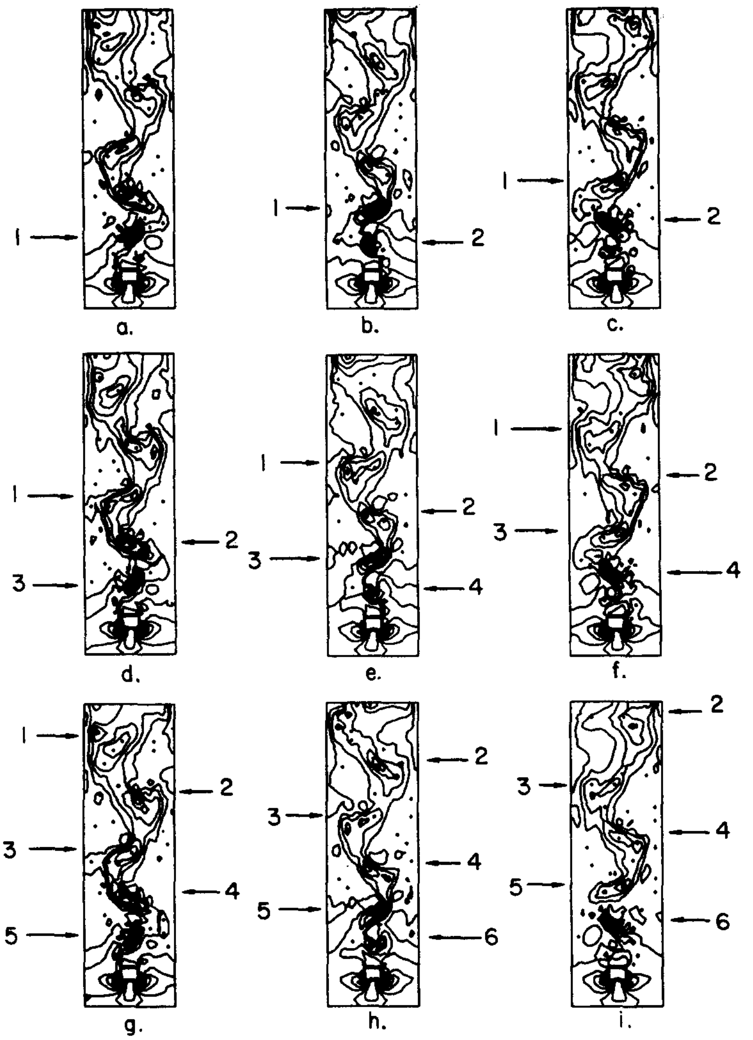

Figure 6. Contour plots of the momentum exchange function at equal time intervals. (a) $t = 2.410$ sec, (b) $t = 2.475$ sec, (c) $t = 2.540$ sec, (d) $t = 2.605$ sec, (e) $t = 2.670$ sec, (f) $t = 2.735$ sec, (g) $t = 2.800$ sec, (h) $t = 2.865$ sec, (i) $t = 2.930$ sec.

frame *f*. In particular, the bubble number density contours for this vortex show the presence of severe fragmentation with two maxima, one persisting as a result of the leading edge shear and the other arising downstream from the trailing edge as a result of shearing forces in the flow-separation vorticity layer [illustrated by the large momentum exchange rate observed near the left trailing edge in figure 6(g)]. Associated with the pair of bubble number density maxima is a broad minimum in the bubble radius. Significant accumulation of gas resulting from reverse centrifuging is confined, however, only to the downstream bubble number density maximum of vortex #5 and does not occur due to the absence of centrifugation from vortical motion in the shear region along the side in agreement with the expected mechanism for accumulation of gas volume fraction.

In the next stage for vortex 5, figure 4(h) demonstrates that the bubble number density maximum retains its duality. The same frame shows that this split persists downstream in vortices 3 and 4. Indeed, frames *a*, *c* and *e* of the figure indicate the duality may occasionally persist all the way to the outlet. Figures 2(h) and 5(h) show that this duality is also reflected in the maximum of the gas volume fraction and in the minimum of the bubble radius. In the case of the gas volume fraction the vortex pair may persist with one maximum predominating and the other riding along as an associated satellite. Figures 12–14 illustrate even more

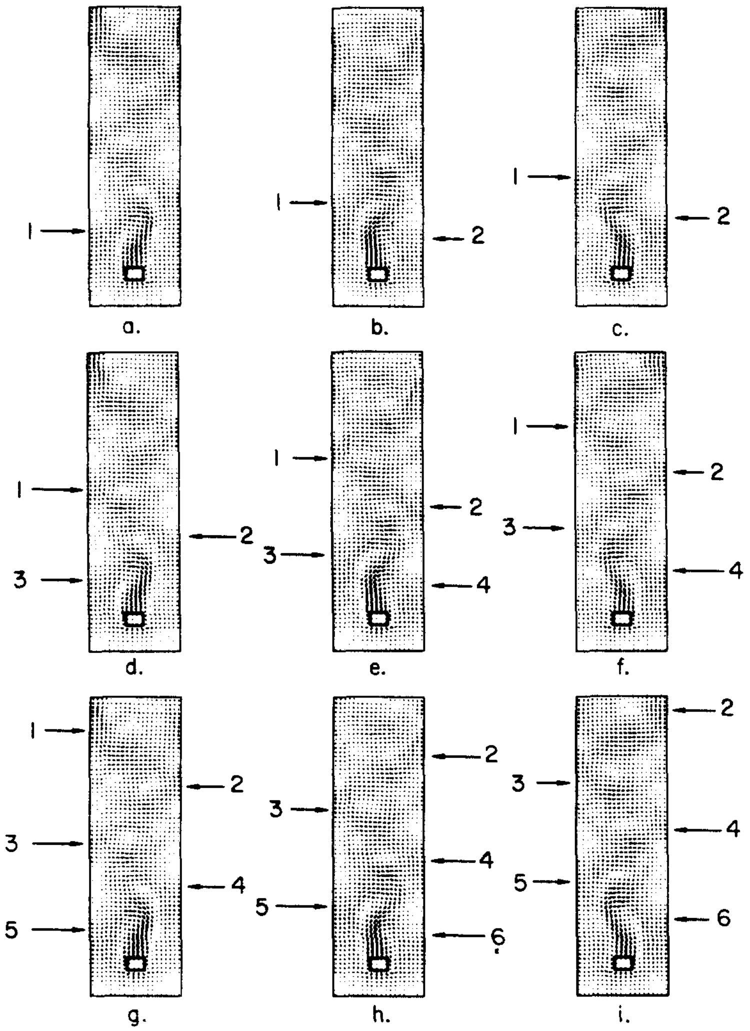

Figure 7. Water velocity vectors referred to a frame moving with the inlet water at equal time intervals. (a) $t = 2.410$ sec, (b) $t = 2.475$ sec, (c) $t = 2.540$ sec, (d) $t = 2.605$ sec, (e) $t = 2.670$ sec, (f) $t = 2.735$ sec, (g) $t = 2.800$ sec, (h) $t = 2.865$ sec, (i) $t = 2.930$ sec.

clearly the nature of this primary/secondary vortex structure as each vortex package propagates downstream. This whole sequence described for vortex 5 on the left side is confirmed for vortex 4 on the right side, whose incipient presence is just becoming visible in figures 4(d) and 5(d).

Regarding the behavior of dynamic pressure during these stages of vortex formation, the closest manifestation of incipient stages is present in figures 3(c) and 3(f) in association with vortices 3 and 5, respectively. The other frames show variations in dynamic pressure lateral to the obstacle, which are dominated by the gradients that accelerate the fluid in such a way as to conserve mass flux in the constricted channels lying between the obstacle and the nearby walls. In other respects the principal features discernable from figure 3 are the pressure minima lying near the center of each vortex. In addition, several frames in figure 3 show anomalous pressure gradients surrounding the upper left and right corners of the calculational region. These pressure extremes result from an intrinsic difficulty in the specification of output boundary conditions for far subsonic flow, but they have a negligible effect on the dynamics as demonstrated by means of an otherwise identical calculation performed using a shorter computing mesh (run 1).

Figures 7 and 8 show that whereas the dominant patterns of the velocity vector fields are nominally the same for gas and liquid at each frame, the detailed picture of the patterns show

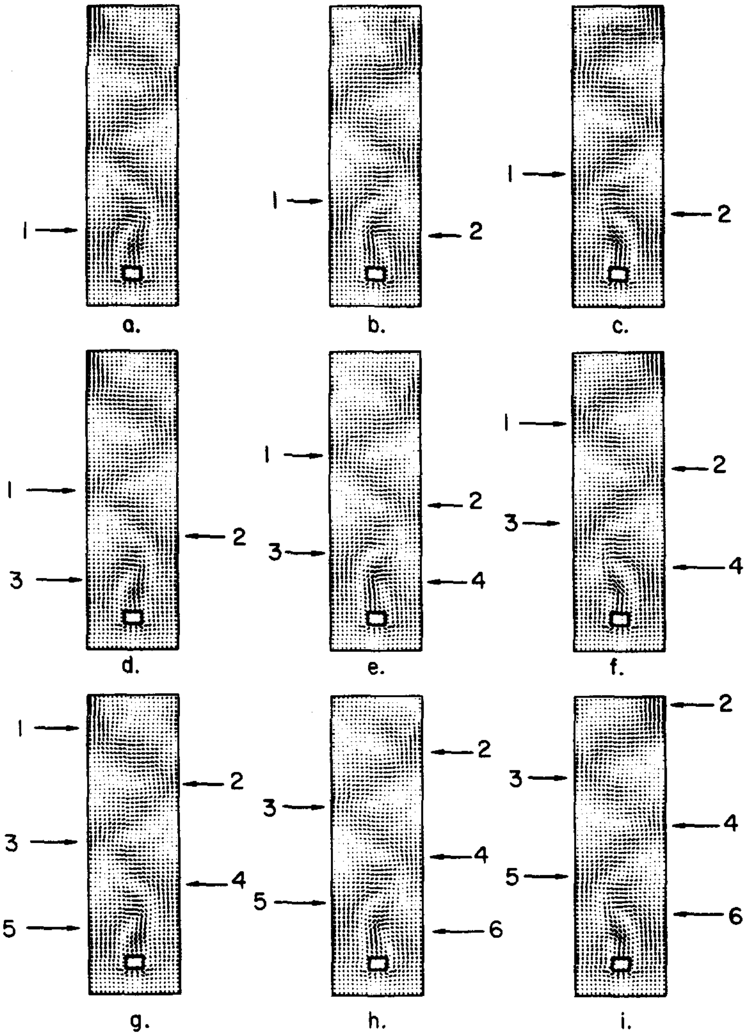

Figure 8. Air velocity vectors referred to a frame moving with the inlet water at equal time intervals. (a) $t = 2.410$ sec, (b) $t = 2.475$ sec, (c) $t = 2.540$ sec, (d) $t = 2.605$ sec, (e) $t = 2.670$ sec, (f) $t = 2.735$ sec, (g) $t = 2.800$ sec, (h) $t = 2.865$ sec, (i) $t = 2.930$ sec.

differences between the two fields, the effects of which are especially evident in such contour plots as those of the momentum exchange function (figure 6). The concentrations of gas volume fraction in figure 2 also result from differences in velocity; in particular, the difference between converging gas velocity towards the center of each vortex and diverging fluid velocity away from the center. Another persistent difference between the two velocity fields is that which is produced by the continuous action of the gas buoyancy relative to the liquid. The local accumulation of gas volume fraction can be expected to produce a buoyancy enhancement to the migration rate for the gas close to that of the bubble rise terminal velocity upstream of the obstacle, which for our bubble size is 25 cm/s. This tendency, however, is mitigated by the increased drag from the smaller bubble size behind the obstacle as shown in figure 15. Less obvious is our observation that the concentration centers, each associated with a vortex, appear to move with an enhanced speed in such a way as to force the more rapid transport of the vortices themselves. For our base case, run 2, we observe that the liquid speed through the stream tube containing the vortices is about 64 cm/s, well below the inlet speed of 90 cm/s. (The apparent discrepancy is resolved by observing that outside of the downstream vortex stream tube the liquid speed is distinctly higher than the inlet speed, in such a way as to give the same volumetric flux as the inflow.) Typical bubble speeds within the vortex stream tube are approximately 85 cm/s and plots of the downstream position of

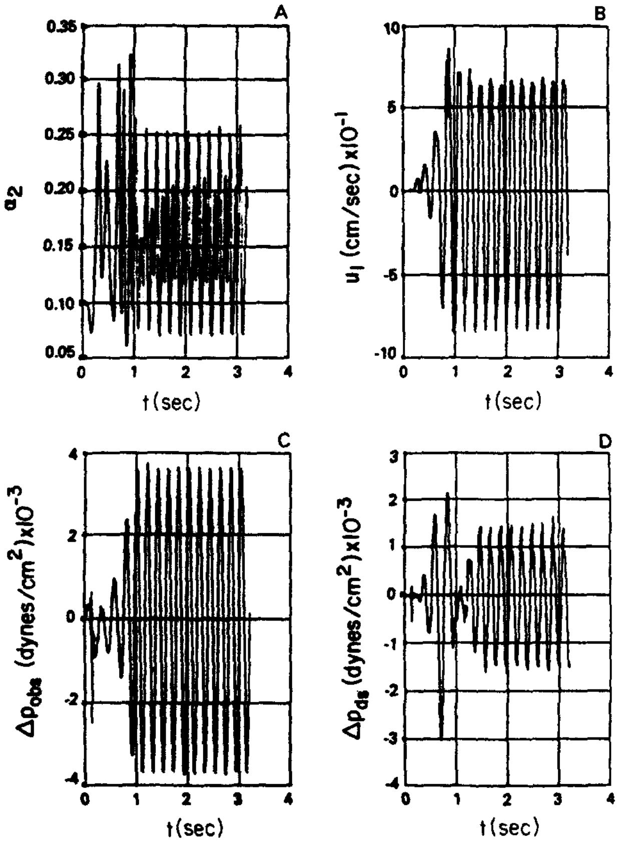

Figure 9. Time-history plots at spatial locations specified in the text.

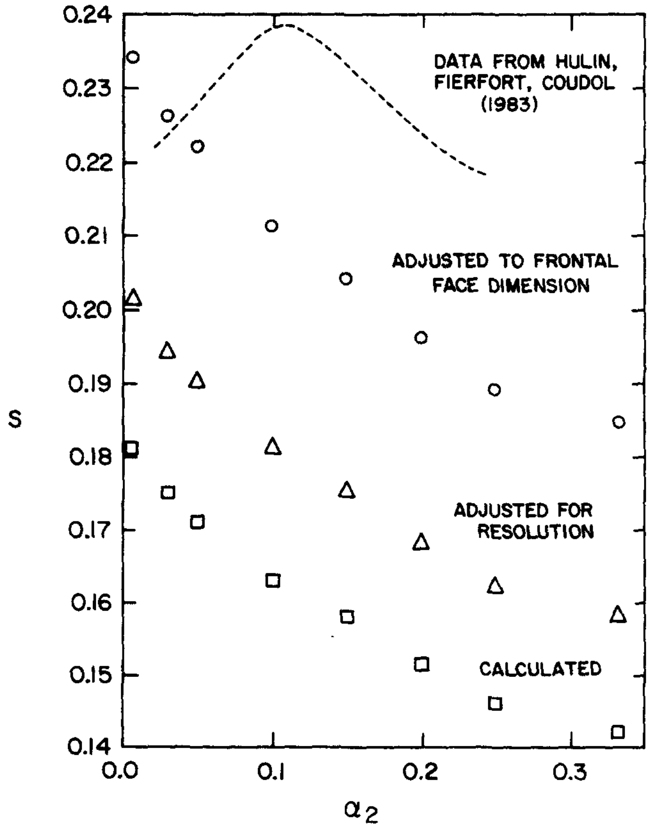

Figure 10. Strouhal frequency dependence on inlet air volume fraction.

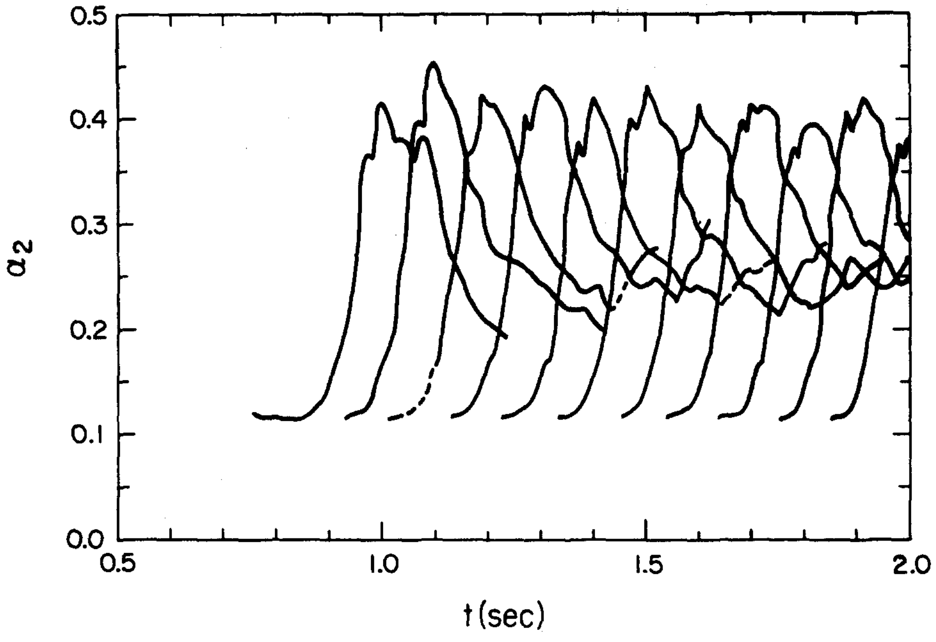

Figure 11. Time evolution of air volume fraction for successive vortices.

concentration center as a function of time show essentially that same speed. The difference between gas speed and fluid speed is thus 20% lower than the initial terminal velocity, consistent with expectations for the smaller bubbles. Motion-picture projection of a time sequence of velocity vectors shows clearly the presence of vortex splitting, in close association with the double peaks of bubble number density described above.

Another feature observed in this study is the presence of a tongue of higher gas volume fraction at the opposite side of the obstacle from the side at which the associated vortex is shed. This tongue structure is especially visible on the right side of the obstacle in figures 2(a), 2(e) and 2(h) and on the left side of figures 2(c) and 2(i).

Figure 9 is a set of time-history plots for α_G, u_L and two transverse pressure differences. In all four plots, the onset of regular oscillatory flow is preceded by an early irregular stage, whose details are not relevant because of the arbitrary nature of the initial conditions. Figures 9(a) and 9(b) show the gas volume fraction and the transverse (horizontal) component of the liquid velocity at a location 5.75 obstacle widths directly downstream and just inside the left-hand corner of the obstacle. The gas volume fraction time history shows the influences of vortices from both sides of the street, as indicated by the double amplitude in the regular oscillatory stage. Figure 9(c) shows pressure difference across the obstacle. Figure 9(d) shows the pressure difference across the same transverse interval 5.75 obstacle widths downstream from the trailing edge.

From these time-history plots we can calculate the Strouhal number, $S = fd/v$, in which it is to be emphasized that d is the geometric width of the obstacle. There is some evidence to suggest that a more appropriate definition of the Strouhal number would be based upon an effective obstacle width, d_e, which would vary not only with Reynolds number, but also with obstacle configuration in such a way that the resulting S would be nearly constant at a value of about 0.23, as discussed below. In experiments with a thin, rectangular object, Fage and Johansen (1927) have shown that the Strouhal number is 0.146 at a Reynolds number of 1.5×10^5. With divergence of the flow in front of the upstream face of their flat plate, it is not surprising that the effective width could exceed the geometric width by the factor $0.23/0.146 = 1.58$.

Lamb (1932) has shown that for the vena contracta the far downstream cross section of a stream bounded by a cavity is 0.611 times the orifice width. If the flow around our flat plate,

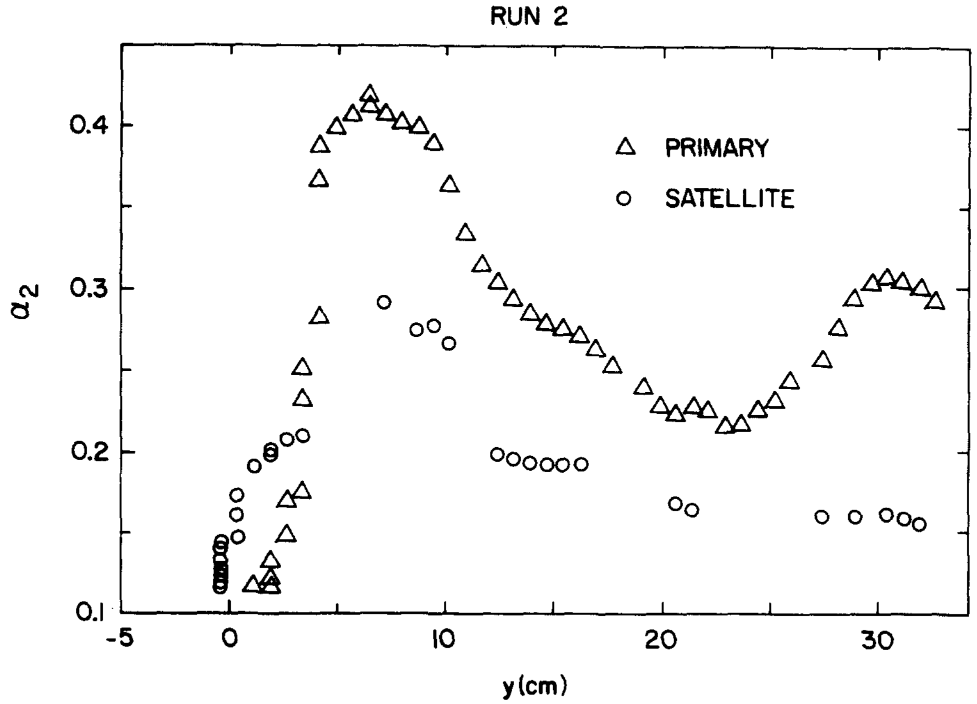

a. VORTEX 2

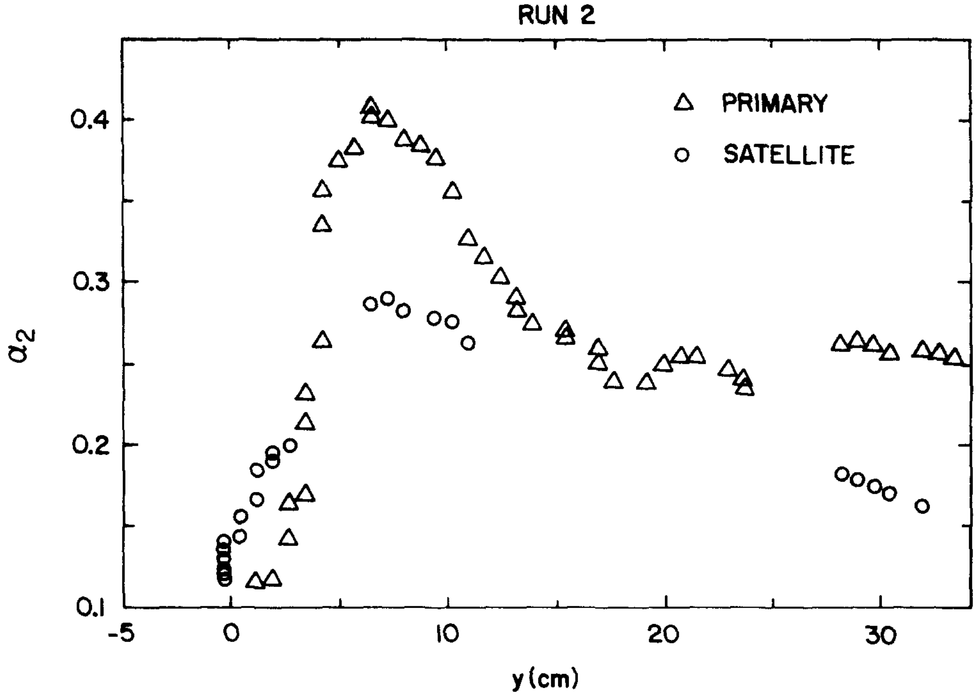

b. VORTEX 3

Figure 12. Air volume fraction of two successive vortices as functions of spatial location.

bounded by rigid walls with a blockage ratio $B = d/W = 1/5$, were ideal (nonviscous) flow with a cavity in the wake of the obstacle then the far downstream width of the flow separation line would be given by $d_e = d\ (0.611 + 0.389/B)$. With a blockage ratio of $1/5$, $d_e/d = 2.556$, which considerably exceeds the factor of 1.58 necessary for the Strouhal frequency factor discussed above. The vena contracta far overcorrects the circumstance for which the

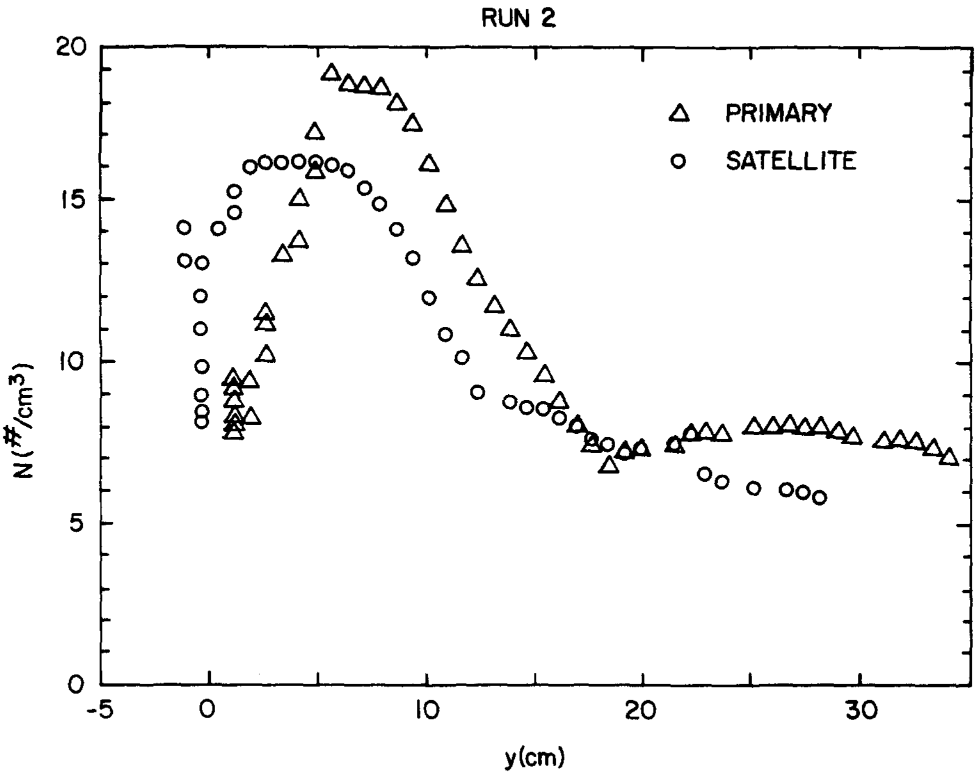

a. VORTEX 2

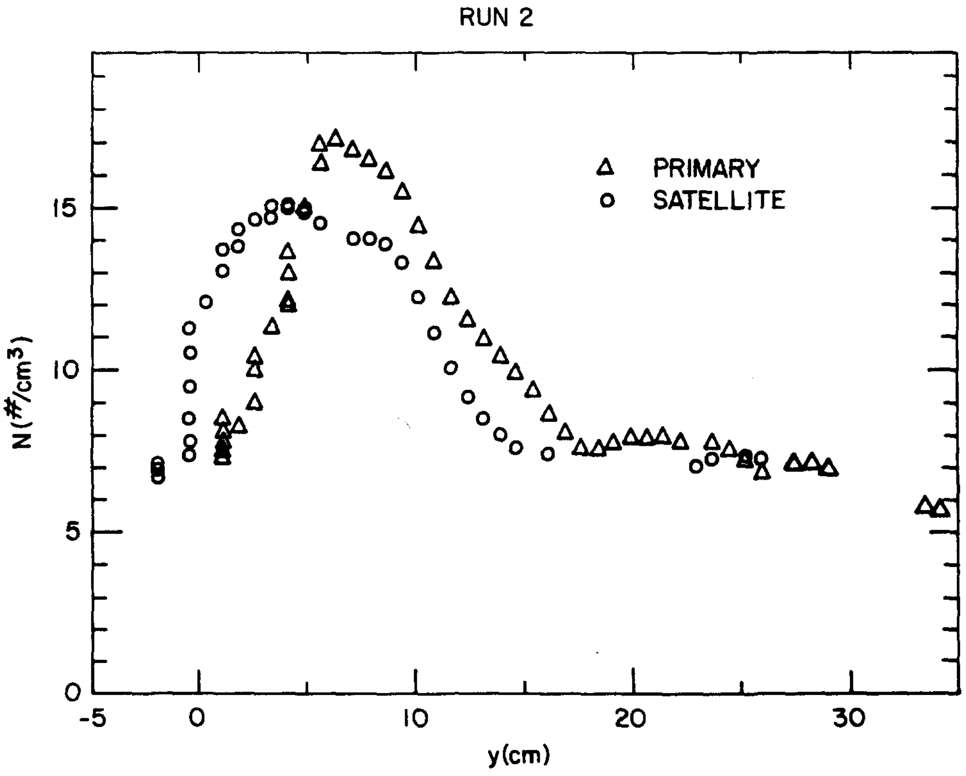

b. VORTEX 3

Figure 13. Bubble number density of two successive vortices as functions of spatial location.

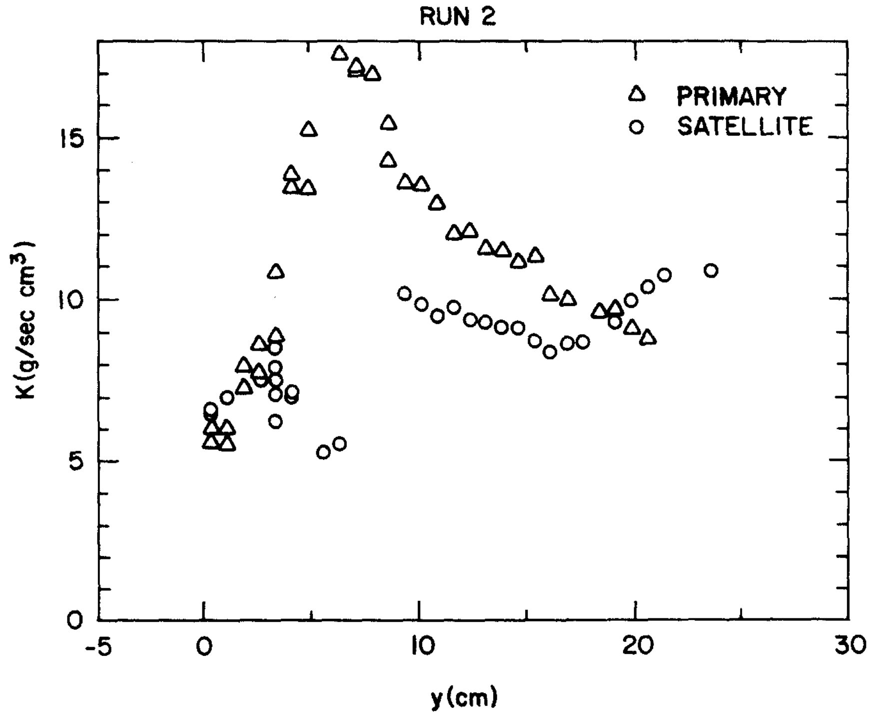

a. VORTEX 2

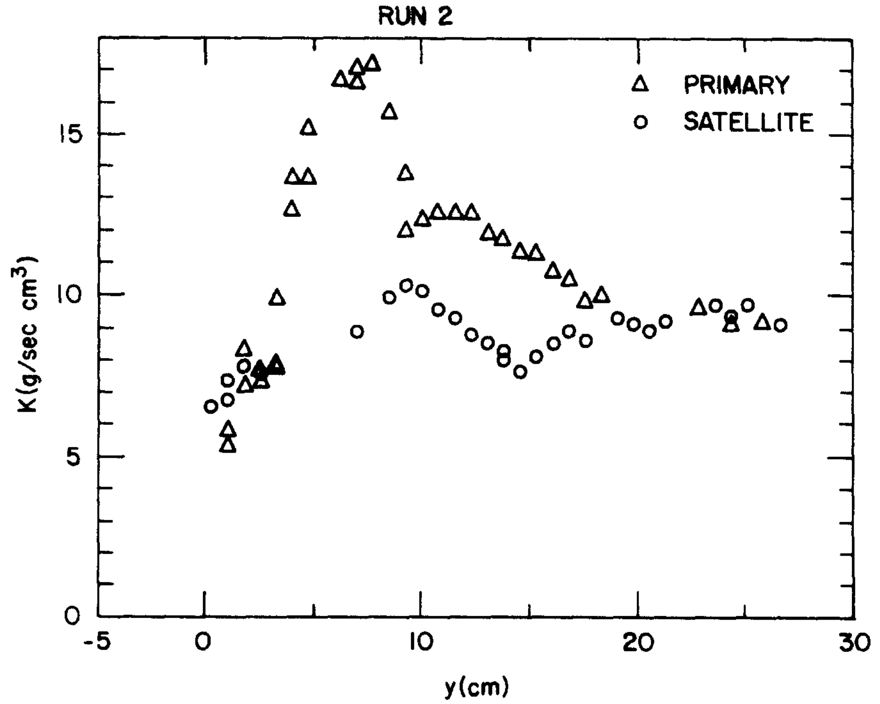

b. VORTEX 3

Figure 14. Momentum exchange function of two successive vortices as functions of spatial location.

appropriate effective width would be governed by the flow field much closer to the plate. Nevertheless, this heuristic observation tends to confirm our premise that there is good potential for expansion of the flow separation line to a width significantly exceeding that of the obstacle itself. For a circular cylinder, (Roshko 1954), the experimentally measured Strouhal number based on the geometric diameter of the cylinder is about 0.204 at a

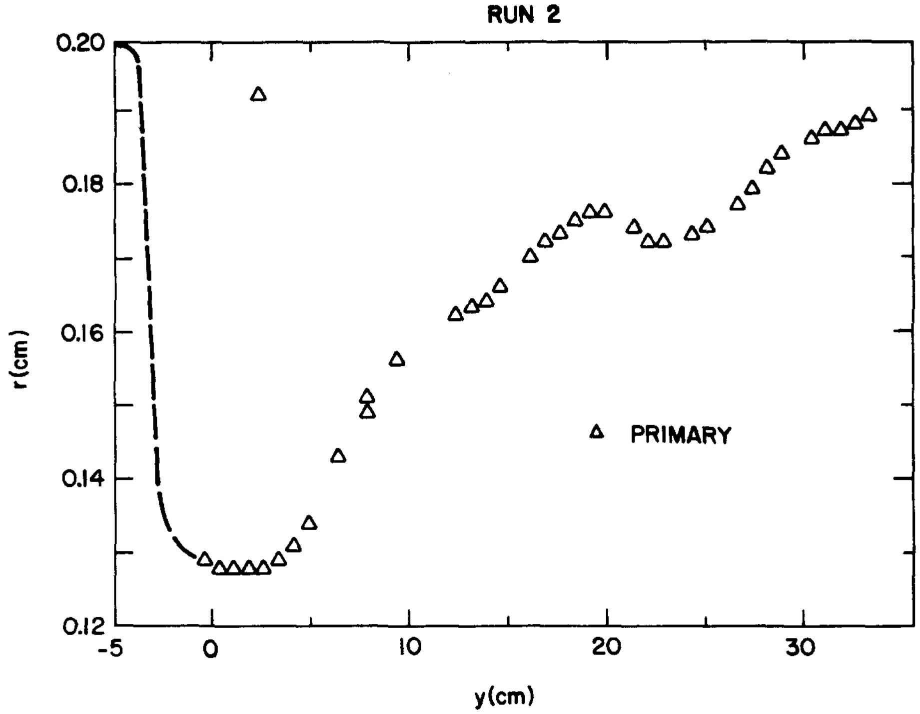

a. VORTEX 2

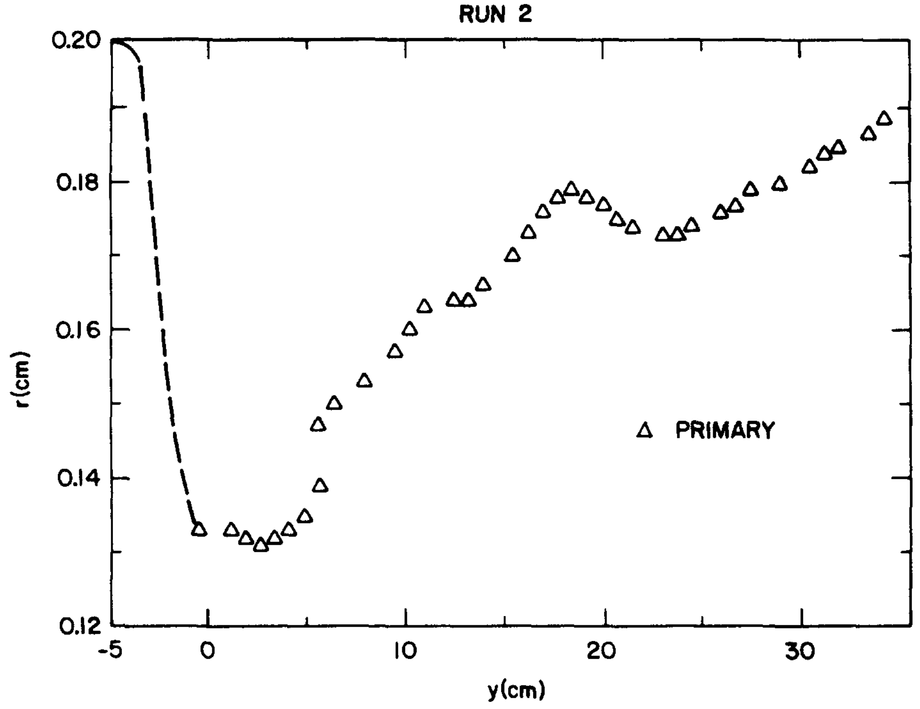

b. VORTEX 3

Figure 15. Bubble radius of two successive vortices as functions of spatial location.

Reynolds number of 300, climbing to an asymptotic value of about 0.210 for higher Reynolds numbers. This result implies an effective obstacle width of $d_e = 0.23/0.204d = 1.13d$, which again is consistent with a slight spreading of the flow separation streamline beyond the geometric width of the cylinder.

The value of effective Strouhal number, 0.23, has been obtained by our performance of

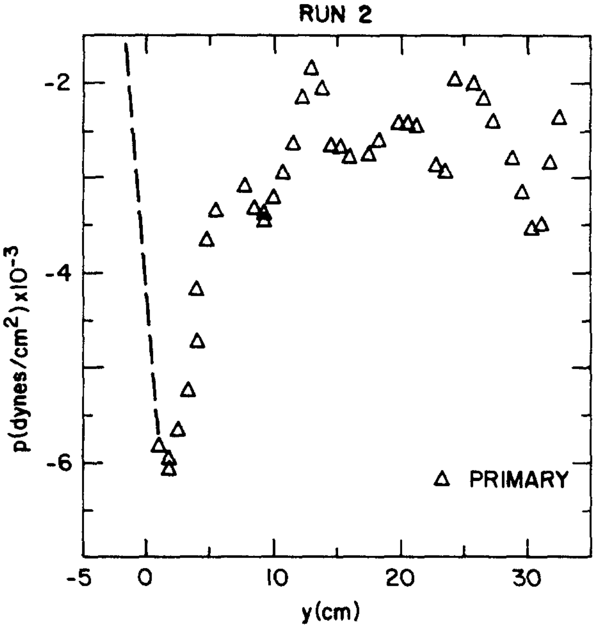

a. VORTEX 2

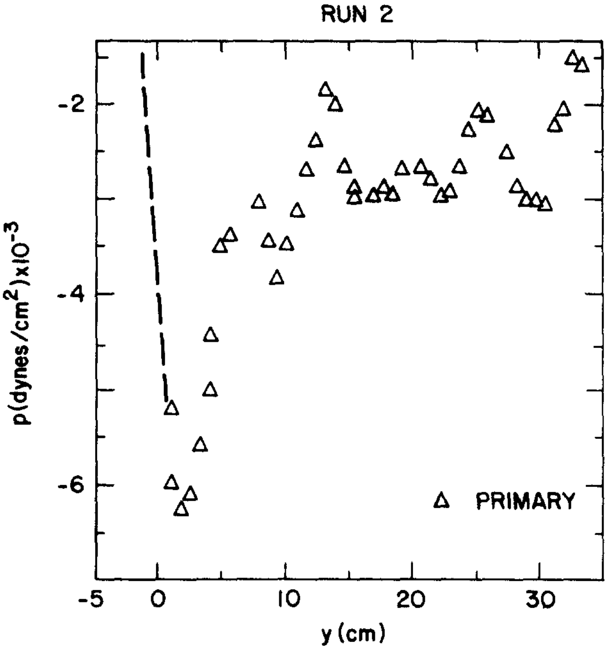

b. VORTEX 3

Figure 16. Dynamic pressure of two successive vortices as functions of spatial location.

some auxiliary, single-phase calculations in which we accomplished the most accurate possible representation of effective width by means of inserting the fluid flow parallel to the sides of a long, rectangular obstacle. Fine resolution calculations yielded $S = 0.23$ at a Reynolds number of 333. With coarser resolution (four finite difference cells across the obstacle), the value was 11% lower. Previous single-phase calculations include those of Fromm & Harlow (1963) in which they examined the flow past a rectangular obstacle and obtained a Strouhal number of 0.137 at a Reynolds number of 300. Accounting for the effects of coarse resolution we can estimate a corrected value of about 0.15 in agreement with the results of Fage & Johansen (1927), and can be scaled to the postulated value of 0.23 in the same way as described for the experiments.

The two-phase calculations in the present study resulted in Strouhal numbers as shown by the □'s in figure 10, indicating a value of 0.181 for $\alpha_{G\text{inlet}} = 0.0$ and dropping uniformly for higher inlet volume fractions to a value of 0.142 at $\alpha_{G\text{inlet}} = 33\frac{1}{3}\%$, the largest inlet volume fraction for which we were able to obtain a (significantly erratic) street. Figure 10 also shows the Strouhal number variation corrected for coarseness of finite difference resolution (the Δ's), as obtained from the auxiliary studies described above. These Strouhal numbers are based on the actual geometric width of the rectangular obstacle used in the calculations. The effective width at the limit of $\alpha_{G\text{inlet}} = 0.0$ is expected to be somewhat larger, as discussed above. For $\alpha_{G\text{inlet}}$ increasing to $33\frac{1}{3}\%$ the uniform drop in Strouhal number is postulated to result from a continually increasing effective width produced by the accumulation of bubbles in the vicinity of the obstacle, as shown in figures 4 and 5.

Directly relevant to these calculations are the experimental results of Hulin *et al.* (1982), which show that the Strouhal number for flow past a trapezoidal object has a magnitude of about 0.220 in the absence of bubbles, rising to about 0.238 for $\alpha_{G\text{inlet}} = 10\%$ and thereafter decreasing until the structure of the street is obliterated at an inlet air volume fraction of about 24%. Their Strouhal number is based on the greatest width of the trapezoid, which lies at the leading upstream edge relative to the incoming flow. These results are shown as a dashed curve in figure 10.

In terms of our interpretation regarding the constant Strouhal number of 0.23 when calculated with effective width, it is apparent that the effective width in the experiments varies from $d_e = (0.23/0.22)d$ for the case of no bubbles to $d_e = (0.23/0.238)d$ at a 10% incoming air volume fraction and thereafter increasing to $d_e = (0.23/0.218)d$ at the largest incoming volume fraction (24%) considered in the experiments. To resolve the apparent paradox demonstrated by this interpretation, we speculate that the trapezoidal shape of the obstacle plays a crucial role in the determination of the effective width. At the pure fluid limit, the downstream contraction of the obstacle apparently decreases the effective width of the flow separation line by an appreciable amount in comparison to our expectations for a thin flat plate. The experimentally increasing Strouhal number indicates that the effect of sparse bubbles is to pull the dividing streamline even closer to the obstacle, ultimately to the extent that the effective width is even less than the geometric width at the leading edge. Because the downstream width of the obstacle is 0.671 of the upstream width, we see that the minimum ratio of d_e/d, equal to 0.97, is less than the contraction that would occur if the dividing streamline were to follow the lateral surfaces. With further increase in the incoming volume fraction of air the tendency reverses, and the effective width ultimately exceeds again the geometric widths at the leading face.

If the Strouhal number results of Hulin *et al.* had been scaled by some intermediate geometric width between those of the leading and trailing faces the curve representing their data in figure 10 would have been shifted downwards. In our calculations, we used a rectangular obstacle with a cross section of 3.0 cm, which lies near the average of their leading edge face ($d = 3.5$ cm) and their trailing edge face ($d = 2.35$ cm). Scaling our results by the factor 3.5/3.0 leads to the o's in figure 10.

Although our result does not exactly agree with the data of Hulin *et al.* the trends of large inlet air volume fraction are closely parallel. To resolve the remaining discrepancy would require a finely zoned calculation of the actual trapezoidal object itself, currently precluded by excessive computer expense.

Figure 11 is a time-history plot of successive vortices shed from alternate sides of the obstacle for a typical street (run 1). The profiles of the successive vortices are very similar to each other; however, we notice that every other vortex (the ones that are shed from the left) has a slightly smaller maximum gas accumulation. This difference results from the initial perturbation used in the calculation to initiate the street, and it disappears at late times.

Figures 12–16 track two successive vortices as they move downstream. Each graph shows the maximum (or minimum) value of the field variable associated with the particular vortex, plotted as a function of distance from the trailing edge of the obstacle. Within each vortex we usually observe two extremes for each field variable and have attempted to identify one of these, denoted by Δ's, as the primary and the other, denoted by o's, as the secondary or satellite. In some cases the differentiation is not clear because the two have briefly coalesced and then reseparated. In others the distinction remains clear despite their apparent merging in figures 12–16. Immediately evident in those figures is the basis for our denoting which extremal is primary and which is secondary; namely, that the primary is the one that reaches the greatest extreme in the entire course of its downstream transport. Where the distinction has been lost due to merging and reseparation, we have identified the primary as the more extreme value after separation.

Figure 12 shows the gas volume fraction for vortices number 2 and 3. The vortex in figure 12(a) originates on the right side of the obstacle; the vortex in figure 12(b), on the left side. Figure 12(a) shows the periodic occurrence of the satellite concentration especially well. As shown in figure 2, vortices shed from the right side of the obstacle tend to exhibit the satellite only on their right side; those shed from the left side likewise have the incipient satellite only on their left side. The paradoxical dominance of the satellite concentration center close to the obstacle is scarcely visible in the contour plots of figure 2, but is abundantly confirmed by a close analysis of the calculational numbers. During the earliest stage of vortex formation, the leading center of concentration is slower to accumulate gas than the trailing center, but rapidly makes up for this slow start by the time the pair has moved appreciably downstream.

In comparing peak gas concentrations in the vortices, Hulin *et al.* (1983) give two datum points that are directly relevant to the present work. They show that the peak local void fraction is 20% for an inlet value of 2.8% and is greater than 40% for inlet values greater than 8.2%. Our calculations for inlet void fractions of 2.8% and 10% show peak accumulations in the vortices of 21% and 42%, respectively.

The periodic appearance and disappearance of the satellite is correlated with a horizontal oscillation of the position of maximum concentration as it moves downstream, with the satellites being detectable principally in that phase of the oscillation that brings the vortex closer to the wall on its shedding side. As shown in figure 12(b) the appearance of the satellite vortex is not necessarily invariable, with vortex 3 displaying a long interval with that feature absent. Another contrast between the concentration variation for vortices 2 and 3 is apparent as each vortex arrives at a distance well downstream from the obstacle. Vortex 2 shows a significant rise in the concentration of its principal maximum at about 30 cm downstream, whereas vortex 3 shows scarcely any rise at all at that same downstream distance. The smallest level of concentration for these two vortices also differs; it appears that the primary and satellite for vortex 3 coalesced at about 15 cm downstream, thereby leveling off the concentration variation at that point. For vortex 2 the primary and satellite remain distinct, allowing the maximum concentration to continue dropping until about 24 cm downstream.

The bubble number density plots for the same two vortices are shown in figures 13(a) and 13(b). As observed in figure 4, the satellite peaks are more pronounced for the number density plots than for the volume fractions; they tend somewhat more to lag the position of the primary peak rather than to lie lateral to it as in figure 2.

Figures 14(a) and 14(b) show the extremes of momentum exchange rate between the two fields for vortices 2 and 3. The significance of momentum exchange is that it indicates the strength of the shear forces exerted on the bubbles by the surrounding liquid, which is closely related to the rate at which the bubbles are fragmented. Although the maximum occurs about 7 cm downstream from the obstacle, the minimum bubble radius [as shown in figures 19(a) and 19(b)] begins to increase at about 3 cm downstream from the obstacle. Resolution of this paradox results from a closer examination of the shearing forces that are very intense along the sides of the obstacle itself although not visible in figure 14, which shows only the vortex related extremes. Thus, the formation of a minimum bubble size occurs before the specific differentiation of the vortices themselves, as indicated by the dashed lines to the left in figure 15. These lines follow the bubble-size behavior along upstream streamlines that ultimately connect with the fluid in the respective vortices. The bubble size drops rapidly from the inlet equilibrium radius (0.2 cm); thereafter, rising rather uniformly toward that same value, which it should ultimately reattain far downstream of the obstacle.

The dynamic pressure associated with the vortices is shown in figures 16(a) and 16(b). The vortex centers are local minima. The lowest pressure occurs in the vortex just after it breaks away from the obstacle. The large pressure gradients lateral to the obstacle produce the large accelerations responsible for the extreme shearing forces described for this region.

D. *Comparisons among the four calculations*

The shortened channel length in run 1 allows us to examine the effect of the outflow boundary condition on the street. Calculational results for run 1 are close to those for run 2, indicating that the far downstream results for concentration behavior (shown in figure 12) are significant.

In run 3 the channel walls are moved outward, changing the blockage ratio. The calculational results of run 3 differ from those of run 2 in several respects. The absolute maximum in the gas accumulation, which occurs shortly after vortex shedding, is greater than the absolute maximum predicted in run 2 by about 7%. The bubble number density is slightly lower in the far downstream region for run 3 than for run 2, and the corresponding bubble radii in run 3 are larger. The street in run 3 is less chaotic, and the bubble radii approach the input equilibrium values more rapidly in the far downstream region. The Strouhal frequency for run 3 is 7% lower than for the other three runs.

In run 2, ω_b is chosen such that relaxation to local equilibrium is very fast relative to the period of the street. Thus, when local conditions favor fragmentation or coalescence, the bubbles respond almost instantaneously. In run 4, the relaxation rate is slower, and the time required for size adjustment is comparable to the period of the street itself. Figure 17 shows

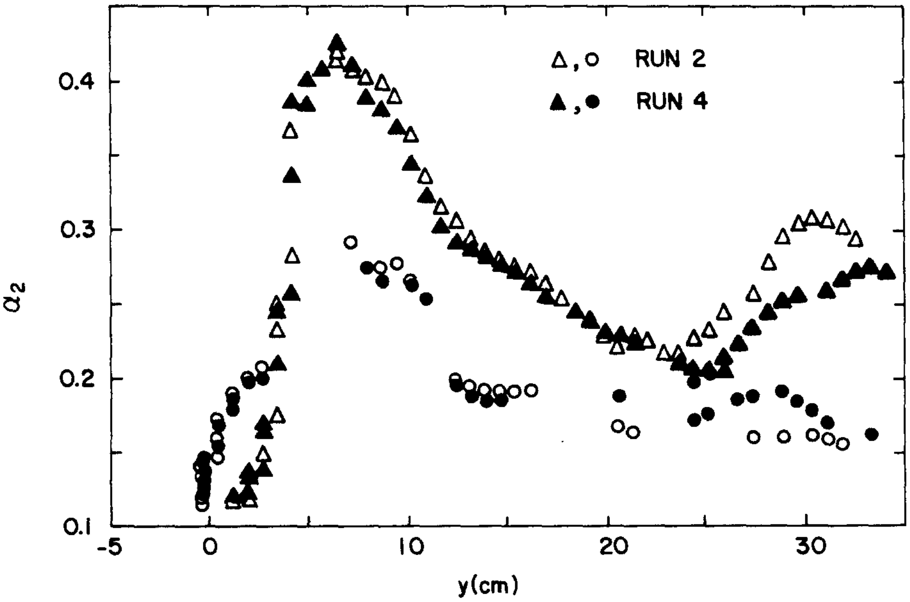

Figure 17. Primary and satellite air volume fraction as functions of spatial location for rapid coalescence/framentation model (run 2) and delayed coalescence/fragmentation model (run 4).

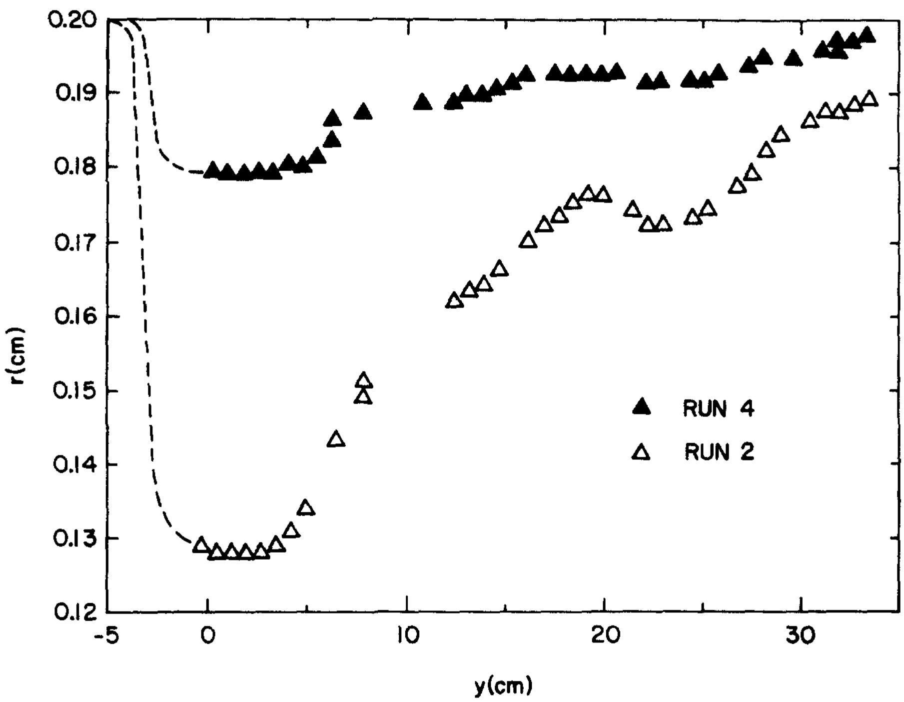

Figure 18. Bubble radius as a function of spatial location for rapid coalescence/fragmentation model (run 2) and delayed coalescence/fragmentation model (run 4).

that the variations in gas-volume fraction are nearly the same for both calculations. However, very different bubble radii (figure 18) and bubble number densities (figure 19) are predicted. The slow accommodation in run 4 results in only a small departure from the inlet value throughout the entire flow region. The corresponding effect on bubble number density is shown in figure 19.

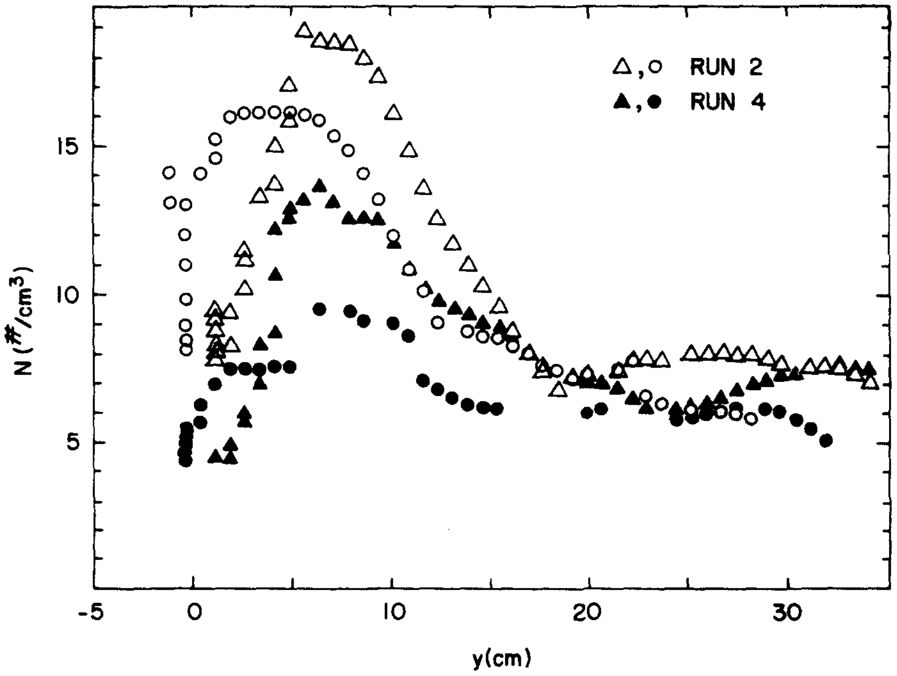

Figure 19. Primary and satellite bubble number density as functions of spatial location for rapid coalescence/fragmentation model (run 2) and delayed coalescence/fragmentation model (run 4).

Acknowledgement—This work was supported in part by funds from the U.S. Department of Energy and in part by funds from Schlumberger-Doll Research.

REFERENCES

ALBORN, F. 1902 Uber den Mechanismus des Hydro-dynamischen Widerstandes. *Abh. Geh. Naturweiss.* **17**.

BEARMAN, P. W., & OBASAJU, E. D. 1982 An experimental study of pressure fluctuations on fixed and oscillating square-section cylinders. *J. Fluid Mech.* **119**, 297–321.

BESNARD, D. & HARLOW, F. H. 1985a Turbulence in two-field incompressible flow. Los Alamos National Laboratory report LA-10187-MS.

BESNARD, D. C. & HARLOW, F. H. 1985b Turbulence in multiphase flow. *Int. J. Multiphase Flow*, in preparation.

COOK, T. L. & HARLOW, F. H. 1984a VORT: A computer code for bubbly two-phase flow. Los Alamos National Laboratory report LA-10021-MS.

COOK, T. L. & HARLOW, F. H. 1984b Virtual mass in multiphase flow. *Int. J. Multiphase Flow*, to be published.

FAGE, A. & JOHANSEN, F. C. 1927 On the flow of air behind an inclined flat plate of infinite span. *Proc. Roy. Soc. (London)* **A116**, 170–197.

FROMM, J. E. & HARLOW, F. H. 1963 Numerical solution of the problem of vortex street development. *Phys. Fluids* **6**, 975–982.

HARLOW, F. H. & FROMM, J. E. 1964 Dynamics and heat transfer in the von Kármán wake of a rectangular cylinder. *Phys. Fluids* **7**, 1147–1156.

HARLOW, F. H. & AMSDEN, A. A. 1975 Numerical calculation of multiphase flow. *J. Comput. Phys.* **17**, 19–52.

HIRT, C. W. 1968 Heuristic stability theory for finite difference equations. *J. Comput. Phys.* **2**, 339–355.

HULIN, J-P, FIERFORT, C. & COUDOL, R. 1982 Experimental study of vortex emission behind bluff obstacles in a gas liquid vertical two-phase flow. *Int. J. Multiphase Flow* **8**, 475–490.

VON KÁRMÁN, TH. & RUBACH, H. 1912 Uber den Mechanismus des Flussigkeits und Luftwiderstandes. *Phys. Zs.* **13**, 49–59.

LAMB, H. 1932 *Hydrodynamics*. Cambridge Univ. Press, Cambridge, MA.

LAUNDER, B. E. & SPALDING, D. B. 1973 The numerical computation of turbulent flows. *Meth. Appl. Mech. Eng.* **3**, 269–289.

LESSEN, M. & SINGH, P. J. 1974 Stability of turbulent jets and wakes. *Phys. Fluids* **17**, 1329–1330.

PEEBLES, F. M. & GARBER, H. J. 1953 Studies on the motion of gas bubbles in liquids. *Chem. Eng. Prog.* **49**, 88–97.

ROSHKO, A. 1954 On the development of turbulent wakes from vortex streets. National Advisory Committee for Aeronautics Report 191.

STROUHAL, V. 1878 Uber eine besondere Art der Tonerregung. *Ann. Phys. Chemie, Neue Folge* **5**, 216–251.

THOMAS, N. H., AUTON, T. R., SENE, K., & HUNT, J. C. R. 1983 Entrapment and transport of bubbles by transient large eddies in multiphase turbulent shear flows. International Conference on the *Physical Modeling of Multiphase Flow*, Coventry, England, 169–184.